Simulation Study of Two-Phase Fluid 3D Imaging Using Lab-on-Chip ECT

Hor Xian Feng[1], Leow Pei Ling[2],
Mohamed Sultan Mohamed Ali[3],
Shahrulnizahani bt Mohammad Din[4]
School of Electrical Engineering
Universiti Teknologi Malaysia
Johor, Malaysia
[1]horxianfeng@gmail.com,
[2]leowpl@utm.my,
[3]sultan_ali@fke.utm.my,
[4]hani-md@utm.my

Jaysuman Puspanathan[5],
Nur Amira Zulkiflli[6]
School of Biomedical Engineering
Universiti Teknologi Malaysia
Johor, Malaysia
[5]jaysuman@biomedical.utm.my,
[6]nuramirazulkiflli@gmail.com

Ruzairi Abdul Rahim[7]
Faculty of Electrical & Electronic
Engineering
Universiti Tun Hussein Onn Malaysia
Johor, Malaysia
[7]ruzairi@uthm.edu.my

Abstract—**Electrical Capacitance Tomography (ECT) is a popular technique for multi-phase fluidic imaging. For the sake of better microfluidics handling within a miniaturized platform, this paper presents a simulation study of a lab-on-chip 3D ECT model with two set of 8-planar-electrode arrays position circularly on the top and bottom layer of the sensing microchamber. The presented simulation studies are to reconstruct the 3D images of a square phantom (water) in a background (air) with different location by using Linear Backward Propagation (LBP) as the image reconstruction algorithm. The simulation results have shown that the proposed lab-on-chip 3D ECT is capable to identify the different position of the phantom.**

Keywords—Lab-on-chip 3D ECT; 3D image reconstruction; linear backward propagation (LBP); simulation; two-phase fluid

I. INTRODUCTION

Microfluidics is referred as fluids which have the volume ranging from micro to pico scale [1]. Due to the high surface to volume ratio characteristic, microfluidics technology enjoys the benefit of being high throughput, which in turn shortens the reaction time and outperforms the classical techniques [2].

In order to ease the handling of microfluidics, lab-on-chip that integrates several laboratorial functions including microfluidics handling, detection, mixing, analysis, filtering, monitoring and separation [3] within a miniaturized platform is introduced. Lab-on-chip is equipped with several elementary microfluidics components, such as micropumps, microchannels, microvalves, junctions, nozzles, and reservoirs to carry out the laboratorial functions that are mentioned above. Lab-on-chip is novel and revolutionary for microfluidics technology due to its compactness, fast sample handling, programmability, straightforward process integration, precise measurements and reduced reagent volume.

Lab-on-chip is broadly applied in biomedical industry, as lab-on-chip can carry out molecular biology experiments [4]. The applications of lab-on-chip in biomedical industry mainly focus on biochemical analysis, biosensor, proteomic and cell research, and drug development [5]. For instance, cell culturing which is useful in studying drugs effect, virus, vaccine, protein therapeutic and cancer, is carried out on the platform of lab-on-chip nowadays, and it is commonly known as microfluidics cell culturing. Microfluidics cell culturing does outperform the conventional cell culturing technique, as it is more flexible in device design, consumes less reagents, yet provides real-time and on-chip analysis [1], [6], [7]. On the other hand, for the past few decades, lab-on-chip provides another alternative for

chemical synthesis [8]. As compared to conventional chemical synthesis, applying lab-on-chip for chemical synthesis is more precise in control, uses less reagent, provides safer experimental environment, and increases energy efficiency (green credentials) [9]. In fact, chemical synthesis is significant in developing organic chemistry, biomedicine and material science [10].

Undoubtedly, imaging of the reactions within the microchamber is important, as it provides vast of information including the location, shape and size of the interested object, which in turn is useful for monitoring and analyzing during experiments. Therefore, lab-on-chip ECT which reconstructs images based on the permittivity distribution is proposed to fulfill the need of fluidic imaging, as different phase of fluids generally have significant difference in their permittivity property. In 2014, Aizat Azmi *et al.* [11] had shown the feasibility of applying planar electrodes for lab-on-chip ECT application. The capacitance measurements provided by planar electrodes are reasonable and have a good agreement with the theoretical calculation. In 2015, Zhen Ren *et al.* [12] had investigated the performance of miniaturized ECT through simulation in four aspects: (1) the effective sensing area, (2) the distance between electrical electrodes, (3) the angle between electrical electrodes, and (4) the number of electrical electrodes. Later, in the year of 2017, Nur Adila [13] had developed a lab-on-chip ECT for two-phase fluidic flow imaging. 8-planar-electrode arrays were applied to reconstruct the image of a 16mm diameter sensing microchamber. The reconstructed images are highly identical to the camera-captured images.

All the latest reported works about lab-on-chip ECT are limited to 2D imaging. As compared to 3D imaging, 2D imaging is poor in visualization and fails to reveal the real situation within the microchamber. This is because 2D imaging is an intuitive display of 3D imaging. Therefore, this paper presents a simulation study of a lab-on-chip ECT model for two-phase fluidic 3D imaging.

II. PRINCIPLE OF ECT

Fundamentally, ECT displays images based on the permittivity distribution within the sensing chamber. The derivation of 3D ECT image reconstruction algorithm could be started from fundamental equation (1), which shows the relationship between capacitance, charge and voltage.

$$C = \frac{Q}{V_c} \qquad (1)$$

where C is the capacitance; Q is the charge; V_c is the voltage applied across the electrodes.

Equation (1) is then derived into equation (2), as charge equals to the volume integration of volume charge density, $Q = \int_v \rho_v(\mathbf{r}) \, dv$.

$$C = \frac{1}{V_c} \int_v \rho_v(\mathbf{r}) \, dv \qquad (2)$$

where $\rho_v(\mathbf{r})$ is the volume charge density; $\int_v \quad dv$ is the volume integration; $\mathbf{r} = (x, y, z)$.

According to Gauss's law (Maxwell's first equation), $\rho_v = \nabla \cdot \mathbf{D}(\mathbf{r})$; therefore, equation (2) is further derived into equation (3).

$$C = \frac{1}{V_c} \int_v \nabla \cdot \mathbf{D}(\mathbf{r}) \, dv \qquad (3)$$

where $\mathbf{D}(\mathbf{r})$ is the electric flux density; $\nabla \cdot$ is the divergence operator.

Equation (3) is derived into equation (4) as $\mathbf{D}(\mathbf{r}) = \varepsilon(\mathbf{r})\mathbf{E}(\mathbf{r})$; equation (4) is then derived into equation (5), as $\mathbf{E}(\mathbf{r}) = -\nabla_\emptyset(\mathbf{r})$.

$$C = \frac{1}{V_c} \int_v \nabla \cdot [\varepsilon(\mathbf{r})\mathbf{E}(\mathbf{r})] \, dv \qquad (4)$$

$$C = -\frac{1}{V_c} \int_v \nabla \cdot [\varepsilon(\mathbf{r})\nabla_\emptyset(\mathbf{r})] \, dv \qquad (5)$$

where $\varepsilon(\mathbf{r})$ is the spatial permittivity distribution; $\mathbf{E}(\mathbf{r})$ is the electric field; $\nabla_\emptyset(\mathbf{r})$ is the potential difference.

According to divergence theorem, equation (5) could be written as equation (6). Divergence theorem states that, $\oint_s \mathbf{A} \, d\mathbf{S}$ equals to $\int_v \nabla \cdot \mathbf{A} \, dv$, where $\oint_s \mathbf{A} \, d\mathbf{S}$ is the net outflow of flux of vector field $\mathbf{A}$ from closed surface; $\nabla \cdot \mathbf{A}$ is the net outflow of flux of vector field $\mathbf{A}$ per unit volume over a closed surface. Therefore, volume integration of $\nabla \cdot \mathbf{A}$ equals to $\oint_s \mathbf{A} \, d\mathbf{S}$.

$$C = -\frac{1}{V_c} \oint_s \varepsilon(\mathbf{r})\nabla_\emptyset(\mathbf{r}) \, d\mathbf{S} \qquad (6)$$

where $\oint_s \quad d\mathbf{S}$ is the closed surface derivation.

$\nabla_\emptyset$ in equation (6) is also a function of ε. Therefore, equation (6) could simplified as equation (7).

$$C = f(\varepsilon) \qquad (7)$$

where f is the non-linear function.

For a more detailed explanation of the fundamental image reconstruction algorithm of ECT, references [14]–[16] can be further referred.

III. 3D ELECTRICAL CAPACITANCE TOMOGRAPHY

A. Modelling of Lab-On-Chip 3D ECT

Fig. 1 illustrates a lab-on-chip 3D ECT model with 8-planar-electrodes arrays on the top and bottom of the sensing chamber. The lab-on-chip ECT model is developed in COMSOL Multiphysics. The height of the model is 1mm, while both the width and length of the model are 5mm. On the other hand, the width and length of the rectangular planar electrodes are 0.4mm and 1.5mm respectively.

In addition, Fig. 2 demonstrates the parts of the lab-on-chip 3D ECT model. The planar electrodes are made by copper, while the container is made by polydimethylsiloxane (PDMS), which is a common fast prototypic material of lab-on-chip devices.
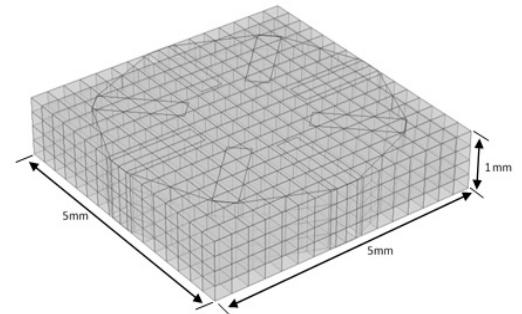

Fig. 1. Schematic diagram of the lab-on-chip 3D ECT model.
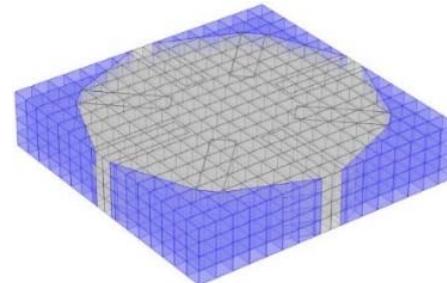

(a)
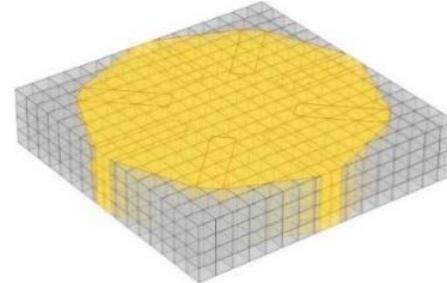
(b)
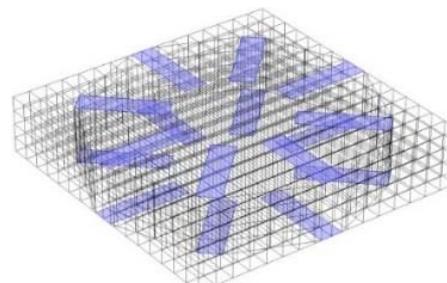
(c)

Fig. 2. Highlighted parts indicate (a) container (b) sensing chamber and (c) planar electrodes of the lab-on-chip 3D ECT model.
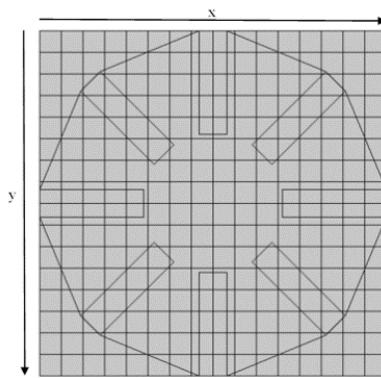
Fig. 3.   X-Y plane of lab-on-chip 3D ECT model.
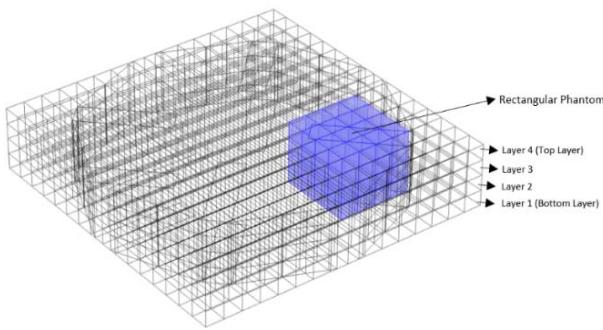
Fig. 4.   Lab-on-chip 3D ECT four layers modelling with single phantom.

At the same time, Fig. 3 shows the X-Y plane of the lab-on-chip 3D ECT model. The resolution of the X-Y plane is 16×16 pixels, which is represented by 256 domains, as illustrated as Fig. 3. Both the width and length of each pixel are 0.3125mm, as the width and length of the X-Y plane are 5mm. Moreover, the height of each pixel is 0.25mm, as the vertical part of the model is divided into four layers as demonstrated as Fig. 4.

The modelling of COMSOL Multiphysics begins with the module selection. Electrostatic module is first chosen. After that, 3D geometry of the lab-on-chip ECT model is drawn as Fig. 1. The material in each domain and the boundary parameters are then defined. Mesh is generated for the finite element calculation. Finally, the global capacitance of each electrode pair is computed and evaluated.

For this paper, air and water which have permittivity value of $1Fm^{-1}$ and $80Fm^{-1}$ respectively are applied within the sensing chamber. At the same time, for mesh generation, option of coarser is chosen for the sake of reasonable computational time. Instead of drawing a round sensing chamber of 5mm diameter, a polygon, which mimics the round shape, is drawn in order to decrease the domains, boundaries, and edges during mesh generation. This is because the process of finite element calculation could be fastened with less domains, boundaries, and edges.

B. 3D Image Reconstruction Method

LBP is applied for image reconstruction, as the computational time is short, yet the algorithm is easy to be understood. Consequently, LBP is commonly applied for real-time dynamic imaging.

For n number of planar electrodes, $m = \frac{n(n-1)}{2}$ is the possible electrode pair for an image made up of total p pixels. The basic LBP algorithm (without truncation or thresholding) for calculating a grey level $g(k)$ for each pixels is

$$g(k) = \frac{\sum_{i=1}^m \lambda_i S_i(k)}{\sum_{i=1}^m S_i(k)} \qquad \text{for } k = 1, \dots, p \qquad (8)$$

where λ_i is the normalized capacitance reading; $S_i(k)$ is the normalized sensitivity map; m is the number of electrode pair. This grey level is supposed to be linearly related to the permittivity, with the lowest and highest permittivity material corresponding to $g = 0$ and $g = 1$ respectively. For detailed derivation of basic LBP equation (8) from equation (7), reference [17] can be referred.

In order to normalize the capacitance reading C_i between electrode pair i, λ_i is calculated as shown as equation (8).

$$\lambda_i = \frac{C_i - C_{i(low)}}{C_{i(high)} - C_{i(low)}} \qquad (9)$$

where C_i is the capacitance reading between electrode pair i; $C_{i(low)}$ is the capacitance reading between electrode pair i when sensor chamber is full of the lowest permittivity material; $C_{i(high)}$ is the capacitance reading between electrode pair i when sensor chamber is full of the highest permittivity material.

The sensitivity map is defined by

$$S_i(k) = \frac{C_i^k - C_{i(low)}}{C_{i(high)} - C_{i(low)}} \qquad (10)$$

where C_i^k is the capacitance reading between electrode pair i when the area of pixel k is full of the highest permittivity material while the rest of the sensing chamber is full of the lowest permittivity material.

For this paper, the sensitivity map of each layer of the bottom 8-planar-electrode arrays is first generated. After that, the sensitivity map of the top 8-planar-electrode arrays directly mirrors the sensitivity map of the bottom 8-planar-electrode arrays. In other words, the sensitivity map of the first layer of the bottom 8-planar-electrode arrays is the same as the sensitivity map of the forth layer of the top 8-planar-electrode arrays; the mirroring of sensitivity map could be achieved as the proposed lab-on-chip 3D ECT model is symmetric in its design. As the result, the time in generating sensitivity map could be shortened. In addition, the total number of electrode pair of this model is 56, as the bottom and the top have 28 electrode pair respectively.

Furthermore, for this paper, the sensitivity map which is generated according to equation (10), is raised to the power of 10 in order to improve the sensitiveness of the map. This is because the reconstructed images could be sharpened with the higher sensitiveness of map. The reconstructed image based on equation (8) would be renormalized again by dividing each pixel with the maximum grey level of the reconstructed image as illustrated as equation (11).

$$g_n(k) = \frac{g(k)}{g_H} \qquad \text{for } k = 1, \dots, p \qquad (11)$$

where $g_n(k)$ is the renormalized grey level of pixel k; g_H is the maximum value grey level among $g(k)$.

TABLE I.   SIMULATION RESULTS OF LAB-ON-CHIP 3D ECT MODEL

	Model	Reconstructed Images			
		Layer 1	Layer 2	Layer 3	Layer 4
i					
ii					
iii					
iv					
v					
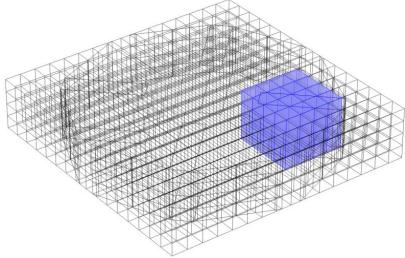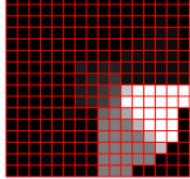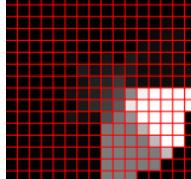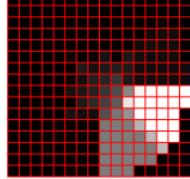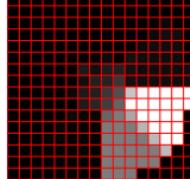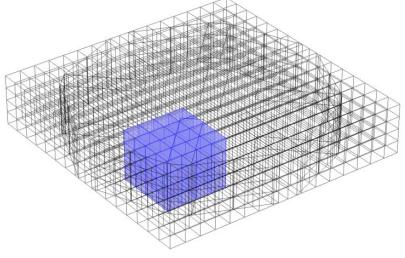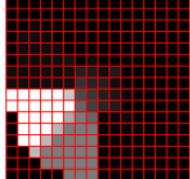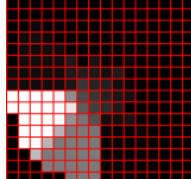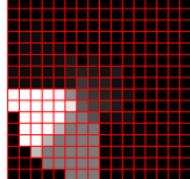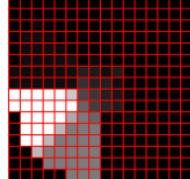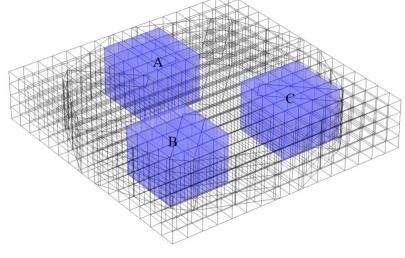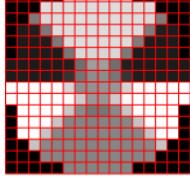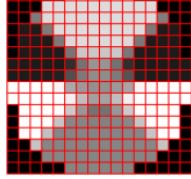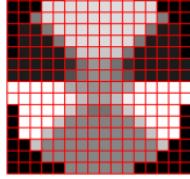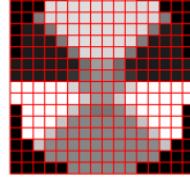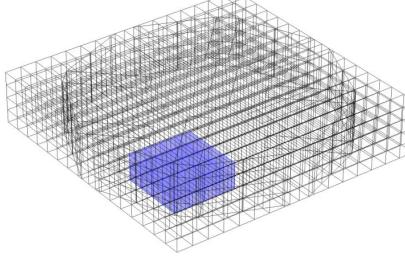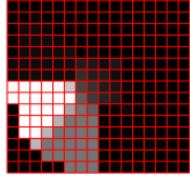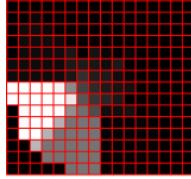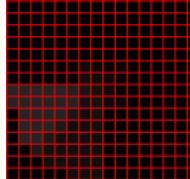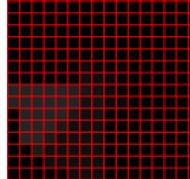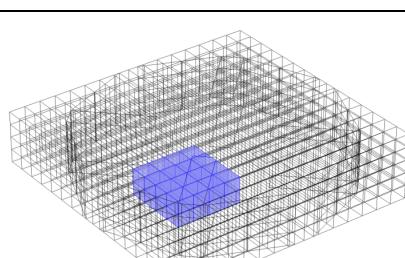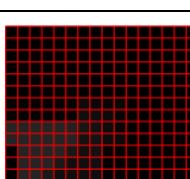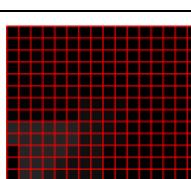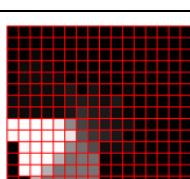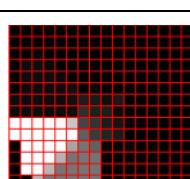
IV. SIMULATION RESULTS

Lab-on-chip 3D ECT modeling and sensitivity map generation are done in COMSOL Multiphysics. On the other hand, LBP is coded in Matlab for image reconstruction. The model is divided into four layers as shown as Fig. 4. Layer 4 is known as the top layer and Layer 1 is known as the bottom layer. The blue-color-highlighted phantom is made up by water, while the rest of the sensing chamber is made up by air. Simulation results are tabulated in TABLE I.

The reconstructed images are greyscale images: the highest permittivity material is displayed in white color and the lowest permittivity material is displayed in black color. Model i, ii and iii have square phantom in all layers; model iv and v have square phantom in layer 1-2 and layer 3-4 respectively.

The simulation results of model i, ii, and iii show that the lab-on-chip 3D ECT is capable to identify the phantom location in X-Y plane. At the same time, the reconstructed images of model iv and v illustrate that the lab-on-chip 3D ECT can recognize the phantom location in different vertical level (different layer) as well. In short, the proposed lab-on-chip 3D ECT model is capable to locate the phantom position in all three dimensions.

On the other hand, the reconstructed images could not restore the shape of the phantom. This is probably due to the ill-posed inverse problem of LBP. LBP suffers the ill-posed inverse problem, as LBP has under-determined equations. Under-determined equations problem is due to the smaller number of measurements than the number of pixels. In addition, LBP itself is very sensitive to noise as well as LBP is a scaled approximation solution. As the result, LBP has no unique solution and is classified as ill-posed mathematically.

For model iii, phantom B and phantom C are close to each other, while phantom A is far to both phantom B and phantom C. Consequently, reconstructed images show that there are ghost images appear between phantom B and phantom C. This is most probably due to the poor accuracy of LBP as well. However, this problem could be solved by applying thresholding in algorithm.

V. CONCLUSION

This paper demonstrated the simulation study of a 3D lab-on-chip ECT model with two set of 8-planar-electrode arrays position circularly on the top and bottom layer of the sensing chamber. The simulation utilized LBP to reconstruct the images of each layer of the sensing chamber. The proposed lab-on-chip 3D ECT model and image reconstruction method were evaluated using square phantom with different position. According to the simulation results, LBP algorithm produces blur shape images of the phantom, but the reconstructed images mapped the phantom position accurately.

REFERENCES

[1] G. M. Whitesides, "The origins and the future of microfluidics," *Nature*, vol. 442, no. 7101, pp. 368–373, Jul. 2006.

[2] N. Convery and N. Gadegaard, "30 years of microfluidics," *Micro Nano Eng.*, vol. 2, no. May 2018, pp. 76–91, Mar. 2019.

[3] A. T. Giannitsis and M. Min, "Usage of microfluidic lab-on-chips in biomedicine," in *2010 12th Biennial Baltic Electronics Conference*, 2010, pp. 249–252.

[4] A. van den Berg, "LABS, cells and organs on chip: Technologies and biomedical applications," in *2017 19th International Conference on Solid-State Sensors, Actuators and Microsystems (TRANSDUCERS)*, 2017, pp. 6–9.

[5] B. Yılmaz and F. Yılmaz, "Lab-on-a-Chip Technology and Its Applications," in *Omics Technologies and Bio-Engineering*, vol. di, Elsevier, 2018, pp. 145–153.

[6] S. Halldorsson, E. Lucumi, R. Gómez-Sjöberg, and R. M. T. Fleming, "Advantages and challenges of microfluidic cell culture in polydimethylsiloxane devices," *Biosens. Bioelectron.*, vol. 63, pp. 218–231, Jan. 2015.

[7] M. Mehling and S. Tay, "Microfluidic cell culture," *Curr. Opin. Biotechnol.*, vol. 25, pp. 95–102, Feb. 2014.

[8] Q. Feng, J. Sun, and X. Jiang, "Microfluidics-mediated assembly of functional nanoparticles for cancer-related pharmaceutical applications," *Nanoscale*, vol. 8, no. 25, pp. 12430–12443, 2016.

[9] K. S. Elvira, X. C. i Solvas, R. C. R. Wootton, and A. J. DeMello, "The past, present and potential for microfluidic reactor technology in chemical synthesis," *Nat. Chem.*, vol. 5, no. 11, pp. 905–915, Nov. 2013.

[10] Y. Liu and X. Jiang, "Why microfluidics? Merits and trends in chemical synthesis," *Lab Chip*, vol. 17, no. 23, pp. 3960–3978, 2017.

[11] A. Azmi, R. Abdul Rahim, P. Song Chee, S. Mohammad Din, N. M. N. Ayob, and P. Ling Leow, "Miniaturized Planar Sensor Development," *J. Teknol.*, vol. 69, no. 8, pp. 101–105, Jul. 2014.

[12] Z. Ren and W. Yang, "A Miniature Two-Plate Electrical Capacitance Tomography Sensor," *IEEE Sens. J.*, vol. 15, no. 5, pp. 3037–3049, May 2015.

[13] N. A. binti M. Razali, "On Chip Planar Capacitance Tomography for Two-Phase Fluid Flow Imaging," 2016.

[14] K. Li and S. Cong, "A review of image reconstruction algorithms in electrical capacitance tomography," in *2018 Tenth International Conference on Advanced Computational Intelligence (ICACI)*, 2018, pp. 128–133.

[15] C. Deyun, S. Dapeng, and L. Letian, "Reconstruction Algorithms Based on Artificial Neural Network for Electrical Capacitance Tomography," in *2008 Second International Symposium on Intelligent Information Technology Application*, 2008, vol. 1, no. 1, pp. 113–117.

[16] K. J. Alme and S. Mylvaganam, "Electrical Capacitance Tomography—Sensor Models, Design, Simulations, and Experimental Verification," *IEEE Sens. J.*, vol. 6, no. 5, pp. 1256–1266, Oct. 2006.

[17] J. C. Gamio, C. Ortiz-Aleman, and R. Martin, "Eelctrical Capacitance Tomography Two-phase Oil-gas Pipe Flow Imaging By The Linear Back-proejction Algorithm," *Geofis. Intenational*, vol. 44, no. 3, pp. 265–273, 2005.